nature materials

Article

https://doi.org/10.1038/s41563-024-02094-6

Dendrite formation in solid-state batteries arising from lithium plating and electrolyte reduction

Received: 30 October 2023

Accepted: 2 December 2024

Published online: 31 January 2025

Check for updates

Haoyu Liu[1,7], Yudan Chen[1,7], Po-Hsiu Chien[1,7], Ghoncheh Amouzandeh[2,3], Dewen Hou[4,5], Erica Truong[1], Ifeoluwa P. Oyekunle[1], Jamini Bhagu[6], Samuel W. Holder[6], Hui Xiong[4], Peter L. Gor'kov[3], Jens T. Rosenberg[3], Samuel C. Grant[3,6] ✉ & Yan-Yan Hu[1,3] ✉

All-solid-state batteries offer high-energy-density and eco-friendly energy storage but face commercial hurdles due to dendrite formation, especially with lithium metal anodes. Here we report that dendrite formation in $Li/Li_7La_3Zr_2O_{12}/Li$ batteries occurs via two distinct mechanisms, using non-invasive solid-state nuclear magnetic resonance and magnetic resonance imaging. Tracer-exchange nuclear magnetic resonance shows non-uniform Li plating at electrode–electrolyte interfaces and local Li^+ reduction at $Li_7La_3Zr_2O_{12}$ grain boundaries. In situ magnetic resonance imaging reveals rapid dendrite formation via non-uniform Li plating, followed by sluggish bulk dendrite nucleation from Li^+ reduction, with an intervening period of stalled growth. Formation of amorphous dendrites and subsequent crystallization, the defect chemistry of solid electrolytes and battery operating conditions play a critical role in shaping the complex interplay between the two mechanisms. Overall, this work deepens our understanding of dendrite formation in solid-state Li batteries and provides comprehensive insight that might be valuable for mitigating dendrite-related challenges.

All-solid-state batteries (ASSBs) are appealing as the leading next-generation technology for electrochemical energy storage with high energy density and enhanced safety. However, their performance is plagued by dendrite-induced short circuits, resulting in limited power densities and shortened lifespans. Dendrite formation in solids differs from that in well-studied liquid systems and presents challenges for non-invasive observation; thus, the mechanisms are unclear. Recent studies have generally focused on examining dendrites formed at the electrode–electrolyte interface[1–10], stemming from non-uniform Li plating and striping[5,7,11–13]. This process is denoted as Mechanism 1 hereafter. Another mechanism based on theoretical investigations suggests that $Li_7La_3Zr_2O_{12}$ (LLZO) surfaces, including grain boundaries, pores and other extended defects, have small bandgaps, which can trap electrons to reduce Li^+ ions[14,15]. Excess electrons on these surfaces have yet to be experimentally validated. In this study, we propose a different mechanism: local reduction of Li^+ to elemental Li^0 at the grain boundaries (Mechanism 2). The conditions triggering dendrite formation via Mechanisms 1 and 2 are distinct. Mechanism 1 is induced by

[1]Department of Chemistry and Biochemistry, Florida State University, Tallahassee, FL, USA. [2]Department of Physics, Florida State University, Tallahassee, FL, USA. [3]Center for Interdisciplinary Magnetic Resonance, National High Magnetic Field Laboratory, Tallahassee, FL, USA. [4]Micron School of Materials Science and Engineering, Boise State University, Boise, ID, USA. [5]Center for Nanoscale Materials, Argonne National Laboratory, Lemont, IL, USA. [6]Department of Chemical and Biomedical Engineering, FAMU-FSU College of Engineering, Florida State University, Tallahassee, FL, USA. [7]These authors contributed equally: Haoyu Liu, Yudan Chen, Po-Hsiu Chien. ✉e-mail: grant@magnet.fsu.edu; yhu@fsu.edu

non-conformal interfacial contact, resulting in non-uniform Li plating at the electrode–electrolyte interface. By contrast, Mechanism 2 sources Li^+ from grain boundaries with dendrites directly forming in the bulk of solid electrolytes. Our study aims to experimentally validate Mechanism 2 and gain a fundamental understanding of its interplay with the more well-known Mechanism 1 during battery cycling. The current approach using electron and optical microscopic techniques[2–7,13,16–22] and neutron-based tools[9,23–26] has generated valuable insights into dendrites formed via Mechanism 1. Yet, information on Mechanism 2 by these techniques is scarce due to their limited penetration depth. Given that the strategies to mitigate dendrite formation for these two mechanisms differ, it is critical to experimentally validate them and determine the dominating mechanism(s) of dendrite formation at different states of charge for ASSBs.

In this study we use a suite of non-invasive techniques to probe dendrites both at the interfaces and in bulk, including solid-state NMR, electron paramagnetic resonance spectroscopy (EPR), tracer-exchange NMR and ex situ and in situ magnetic resonance imaging (MRI), in conjunction with electron microscopic and electrochemical measurements. This comprehensive approach allows us to investigate dendrite formation within ASSBs quantitatively and non-destructively with both spatial and temporal resolution.

Oxide-based solid electrolytes are favoured for their cost effectiveness, as well as chemical and electrochemical stability. LLZO is a prime example, with an ionic conductivity of ~1 mS cm^{-1}, stability against air and H_2O and a wide electrochemical window[27–29]. However, its abundant grain boundaries and limited electrode wettability make it prone to dendrite formation. LLZO serves as a representative system to delve into dendrite formation mechanisms in three-dimensional (3D) solids, uncovering their origins and assisting dendrite mitigation strategies.

Our primary focus is symmetric batteries comprising Li metal electrodes and LLZO electrolytes. In this work, we experimentally validate dendrite formation via Li^+ reduction at grain boundaries (Mechanism 2) and confirm that Mechanisms 1 and 2 dominate at different charge stages. The 3D ^{7}Li MRI reveals Mechanism 1 dendrites cluster at electrode–electrolyte interfaces and propagate via defects, while Mechanism 2 dendrites form small filaments scattered within the electrolyte bulk. In situ quantitative ^{7}Li MRI at an ultra-high field of 21.1 T provides improved sensitivity and temporal resolution, allowing us to dissect dendrite formation kinetics at various locations and charge states.

Ex situ characterizations of dendrites in LLZO

Cubic LLZO (Supplementary Fig. 1) was obtained via solid-state synthesis[27]. We fabricated a symmetric Li/LLZO/Li battery using a 4.8-mm-diameter and 1.0-mm-thick LLZO pellet (Fig. 1a). After initial polarization with a 0.1 mA cm^{-2} current, a smooth electrochemical profile was observed for 7.6 days before voltage destabilization and eventual short circuit (Fig. 1b). To probe dendrites formed in LLZO at different stages of charge, we carried out ex situ magic-angle-spinning (MAS) NMR and EPR experiments. Moderately cycled LLZO (~2 days) exhibited a weak ^{7}Li NMR resonance at ~264.1 ppm (Fig. 1c, middle, and Supplementary Fig. 2), indicating metallic Li^0 formation. This was further confirmed by EPR[30,31] (Fig. 1d, middle).

The hard-shorted LLZO reveals a strong metallic Li^0 signal (Fig. 1c, top) with a slightly larger Knight shift of ~264.5 ppm, suggesting changes in the density of states at the Fermi level and enhanced electron percolation in the dendrite[32]. Concurrently, the narrow line-width of the intense EPR signal (Fig. 1d, top) indicates a morphological shift from mossy to dendritic[31]. Upon removing the Li metal electrodes from the shorted Li/LLZO/Li cell (Methods contains the procedure), the LLZO pellet surfaces reveal dark streaks[2] (Fig. 1e). The lower surface shows fewer streaks than the upper, indicating non-symmetric and non-uniform dendrite growth. Dark spots are visible in the bulk of the retrieved LLZO pellet (Fig. 1f). Post-mortem scanning electron microscopy (SEM) analysis (Fig. 1g) on the cross-sections of the shorted LLZO shows that the Li^0 network grows along the grain boundaries, consistent with previous reports[2]. Ex situ high-resolution and energy-filtered transmission electron microscopy (TEM) of the shorted LLZO confirms the formation of Li dendrites along grain boundaries (Fig. 1h). Dendrites are also observed at some grain boundaries in the moderately cycled LLZO, although they are less prevalent than in the shorted LLZO (Fig. 1i). These post-mortem images (Fig. 1e–i) and the spectroscopic data (Fig. 1c,d) provide a preliminary but incomplete view of dendrite formation within Li/LLZO/Li. To understand dendrite formation in ASSBs comprehensively, it is essential to conduct experimental investigations on intact batteries, integrating spatial and temporal resolution.

Validation of dendrite formation via electrolyte reduction

It is crucial to identify dendrite origins in solids: Mechanism 1 (non-uniform plating at electrode–electrolyte interfaces) versus Mechanism 2 (electrolyte reduction in the bulk). Since the Li^+ source differs between these two mechanisms, we performed ^{6}Li–^{7}Li tracer-exchange NMR to differentiate them. As depicted in Fig. 2a,b, for all the ^{6}Li → ^{7}Li tracer-exchange NMR experiments, the Li metal electrodes are enriched with ^{6}Li (95% ^{6}Li, 5% ^{7}Li), while LLZO contains Li with a natural mix of isotopes (7.5% ^{6}Li, 92.5% ^{7}Li). This difference in ^{6}Li and ^{7}Li isotope abundance between the Li metal electrodes and LLZO is essential for distinguishing the two dendrite formation mechanisms using tracer-exchange NMR. In Mechanism 1, dendrite formation starts with uneven Li plating at the electrode–electrolyte interface, where the ^{6}Li/^{7}Li composition should resemble that of LLZO at the interface. Consequently, dendrites formed via Mechanism 1 are expected to exhibit a ^{6}Li isotope abundance (atomic %), $\frac{^6\mathrm{Li}}{^6\mathrm{Li}+^7\mathrm{Li}} \times 100$, lower than or equal to that of ^{6}Li metal electrodes but higher than or equal to that of LLZO. In Mechanism 2, dendrites form via Li^+ reduction of the grain boundaries in the LLZO electrolyte; therefore, the ^{6}Li isotope abundance in dendrites should be equal to that of grain boundaries in LLZO. Our ^{6}Li–^{7}Li tracer-exchange NMR shows that the ^{6}Li isotope abundance in the grain boundaries is lower than that of grains (Supplementary Fig. 3) due to slower Li diffusion at grain boundaries[33]. Therefore, dendrites formed through electrolyte reduction at grain boundaries (Mechanism 2) are expected to have a ^{6}Li isotope abundance lower than the LLZO average.

Through the ^{6}Li–^{7}Li tracer-exchange process driven by a biased potential across a ^{6}Li/LLZO/^{6}Li symmetric cell, net ^{6}Li flows from ^{6}Li metal electrodes to LLZO while net ^{7}Li migrates from LLZO to ^{6}Li metal electrodes until an equilibrium is reached, where ^{6}Li isotope abundance is the same in the Li metal electrodes and the LLZO (Supplementary Fig. 4). For each round of such a tracer-exchange process, the ^{6}Li isotope abundance in Li metal electrodes (x_1') and LLZO electrolyte (x_2') can be determined with equations (1) and (2), where m_1 is the total Li^+ amount in Li metal electrodes, m_2 is the total Li^+ amount in LLZO electrolyte and n is the amount of Li^+ participating in the tracer-exchange process.

$$x_1' = x_1 - \frac{nm_2}{m_1(m_2+n)}(x_1 - x_2) \quad (1)$$

$$x_2' = x_2 + \frac{n}{m_2+n}(x_1 - x_2) \quad (2)$$

We performed numerical calculations based on equations (1) and (2) using in-house Python codes with starting values of x_1 and x_2 equal to the initial ^{6}Li isotope abundance in Li metal electrodes and LLZO solid electrolytes. The number of iterations equals the number of electrochemical cycles. Results are shown in Fig. 2d, illustrating the gradual convergence of the ^{6}Li isotope abundance in Li metal electrodes and LLZO.

https://doi.org/10.1038/s41563-024-02094-6

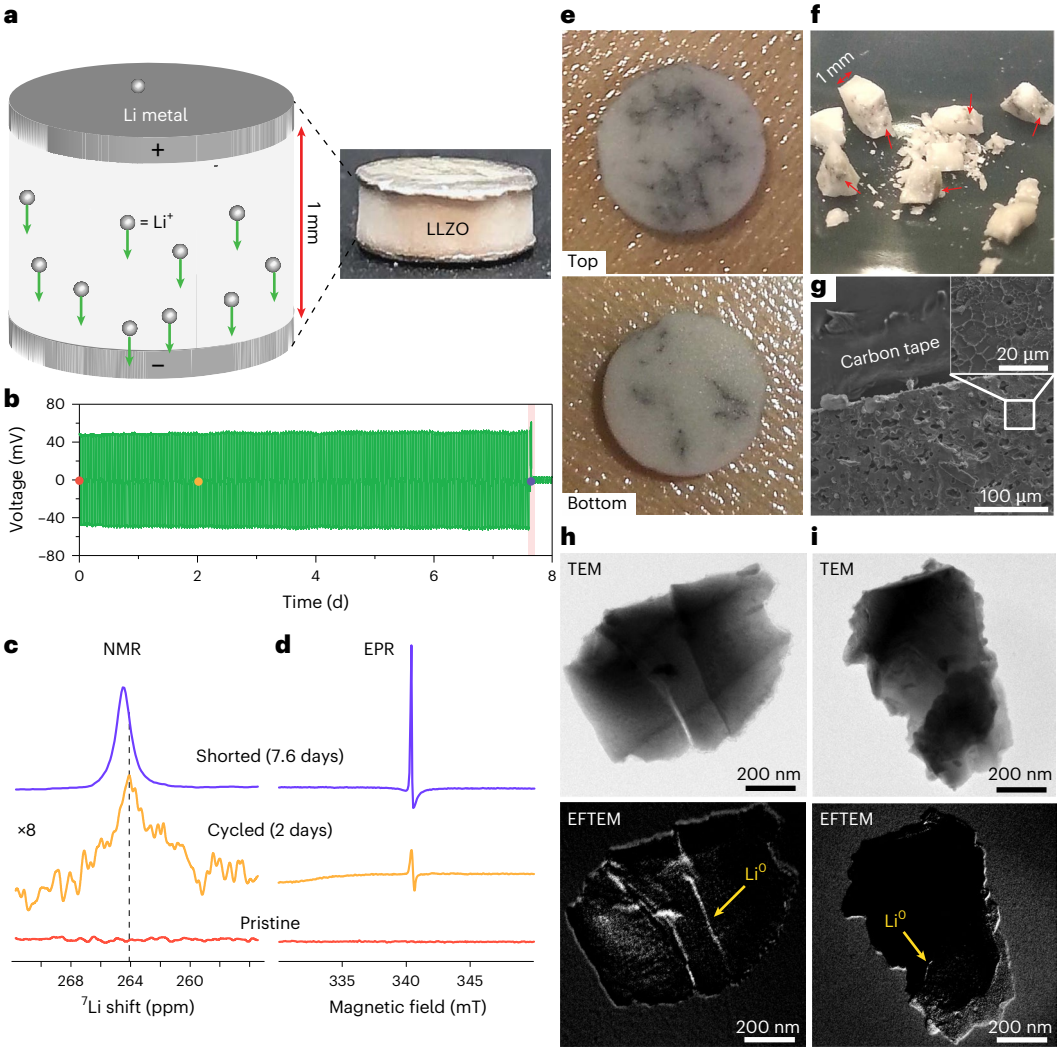

Fig. 1 | Li microstructure formation in cubic LLZO. a, Schematic illustration of a symmetric Li/LLZO/Li battery cell and a digital picture of an actual cell used in this study. **b**, Voltage profile of the Li/LLZO/Li cell polarized with a current density of 0.1 mA cm^{-2}. A short circuit occurs in the shaded region. **c**,**d**, ^{7}Li MAS (25 kHz) NMR (**c**) and EPR (**d**) spectra of Li dendrite formed at three stages—pristine, cycled for two days and shorted—with colours corresponding to the points marked with colour-coded dots in **b**. **e**, Top and bottom view of a shorted LLZO pellet. **f**, Crushed LLZO pellet with cross-sections showing embedded Li microstructures; selective locations are marked with red arrows. **g**, SEM images of the cross-sections from the shorted LLZO pellet; the inset shows a zoomed-in view. **h**, TEM (top) and energy-filtered TEM (EFTEM; bottom) images of the shorted LLZO pellet. **i**, TEM (top) and energy-filtered TEM (bottom) images of the moderately cycled LLZO pellet.

To experimentally determine the ^{6}Li isotope abundance in Li metal electrodes and LLZO at different states of charge, the ^{6}Li/LLZO/^{6}Li symmetrical batteries were electrochemically cycled to a target total charge, and we used ^{6}Li and ^{7}Li MAS NMR to characterize the cycled LLZO and dendrite formed within. As shown in Fig. 2c, the ^{6}Li (top) and ^{7}Li (bottom) NMR spectra of the dendrite (left; 264.5 ppm) and the LLZO (right; 1.2 ppm) exhibit progressive changes as one increases the total charge from 5 coulombs (C) to 24, 61 and 122 C. The ^{6}Li isotope abundance in Li dendrites was then calculated based on quantitative areal integrals of ^{6}Li and ^{7}Li NMR signals, with a calibration factor accounting for the sensitivity difference of ^{6}Li and ^{7}Li NMR (see Methods for details). The quantified ^{6}Li isotope abundance in dendrites and LLZO as a function of total charge (C) is shown in Fig. 2d. The ^{6}Li isotope abundance in the LLZO electrolyte increases as a result of ^{6}Li → ^{7}Li tracer exchange, consistent with the numerical simulation. Since the ^{6}Li isotope abundance in the LLZO and Li metal electrodes is interdependent, the experimental results on the LLZO electrolyte indirectly validate the ^{6}Li isotope abundance in Li metal electrodes obtained from the simulation. The ^{6}Li isotope abundance within the initially formed dendrites lies between that found in LLZO and the Li metal electrodes. This aligns with the anticipated ^{6}Li isotope abundance when dendrites form at the electrode–electrolyte interface through Mechanism 1. Subsequently, as the total charge increases, the ^{6}Li isotope abundance within the dendrites decreases, eventually reaching parity and falling below that of LLZO. The observation that the ^{6}Li isotope abundance of the dendrites becomes less than that found in LLZO in the later stage of cycling provides vital experimental evidence for dendrite formation via Mechanism 2 at LLZO grain boundaries. The simulation and experimental data in Fig. 2d reveal that at the early stage, dendrites primarily form via Mechanism 1, while Mechanism 2 becomes more prevalent in later stages. Additionally, we have sampled the dendrites formed in the middle layers of a LLZO pellet retrieved from a ^{6}Li/LLZO/^{6}Li battery cell cycled to 30 C, which exhibited only a ^{7}Li NMR signal with no ^{6}Li, whereas the LLZO pellet itself shows strong ^{6}Li and ^{7}Li NMR peaks (Fig. 2e); this suggests that Mechanism 2 is the major contributor to the dendrite formation in the middle layers of the LLZO pellet at this cycling stage.

Three-dimensional mapping of dendrites in LLZO

To probe the spatial distribution of dendrites, we conducted 3D ^{7}Li MRI experiments on LLZO and dendrites from Li/LLZO/Li batteries with

https://doi.org/10.1038/s41563-024-02094-6

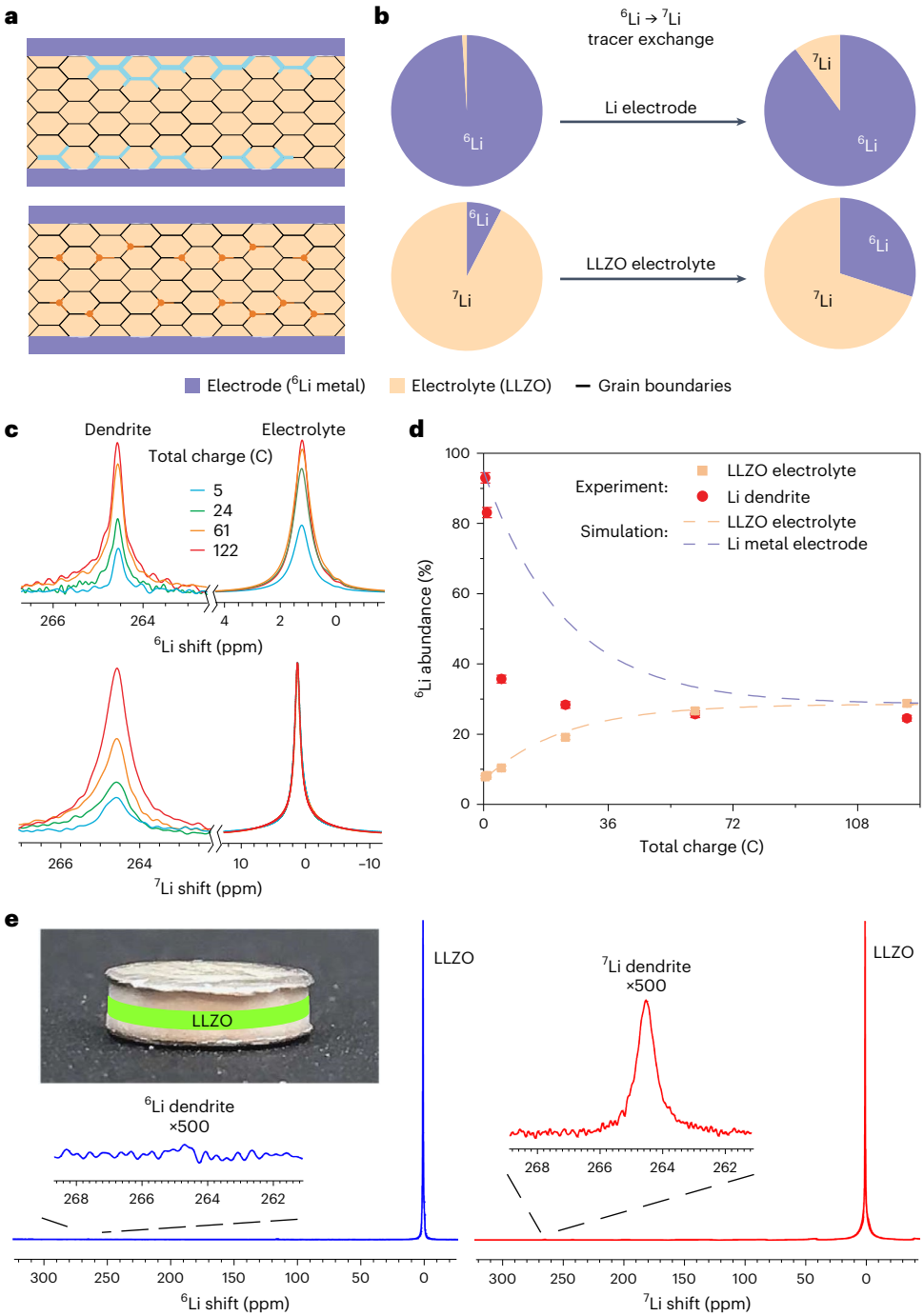

Fig. 2 | Two mechanisms of dendrite formation in LLZO validated via tracer-exchange NMR. a, Schematic illustration of dendrite formed at the electrode–electrolyte interface via non-uniform lithium plating (Mechanism 1, top, dendrite represented as blue lines) and within the bulk electrolyte via Li^+ reduction at grain boundaries (Mechanism 2, bottom, dendrite represented as orange dots at grain boundaries). Tracer-exchange NMR requires ^{6}Li-enriched Li metal electrodes (purple rectangles) and natural-abundance ^{6,7}Li in the LLZO electrolyte (beige rectangles, with the grains of the electrolyte shown as hexagons). Due to the spatial disparity of ^{6,7}Li distribution in this set-up, dendrites formed via Mechanism 1 are relatively ^{6}Li rich, while those formed via Mechanism 2 are ^{7}Li rich. **b**, Schematic illustration of the anticipated changes in the ^{6}Li and ^{7}Li contents of the Li metal anodes (top) and LLZO solid electrolytes (bottom) over the tracer-exchange process. **c**, The ^{6}Li (top) and ^{7}Li (bottom) NMR spectra of LLZO electrolyte and dendrites formed within it after a total charge of 5, 24, 61 and 122 C. **d**, Experimentally quantified results and the numerical simulation on the ^{6}Li abundance in the LLZO electrolyte and Li metal electrodes as a function of total charge. All the experimental data points are reproduced with three battery cells. The error bars are calculated based on the standard deviation of the measured results. The measure of centre for error bars is the mean of the measured results. **e**, The ^{6}Li and ^{7}Li NMR spectra of the middle section of a LLZO pellet (highlighted in green in the inset photo) retrieved from a ^{6}Li/LLZO/^{6}Li battery cell cycled to 30 C. The inset plots show zoomed-in views.

natural-abundance Li isotopes in all the cell components at three cycling stages: pristine, moderately cycled and short-circuited (Fig. 3a). The corresponding voltage profile is shown in Supplementary Fig. 5. MRI measurements are element specific and isotope specific. Along with chemical shift imaging, we can isolate dendrite images from other Li-containing species due to the large separation of the dendrite signal (~264.5 ppm) from that of LLZO (~1.2 ppm). The ^{7}Li MRI images of LLZO and dendrites are superimposed and shown in grey and blue (Fig. 3a), respectively.

https://doi.org/10.1038/s41563-024-02094-6

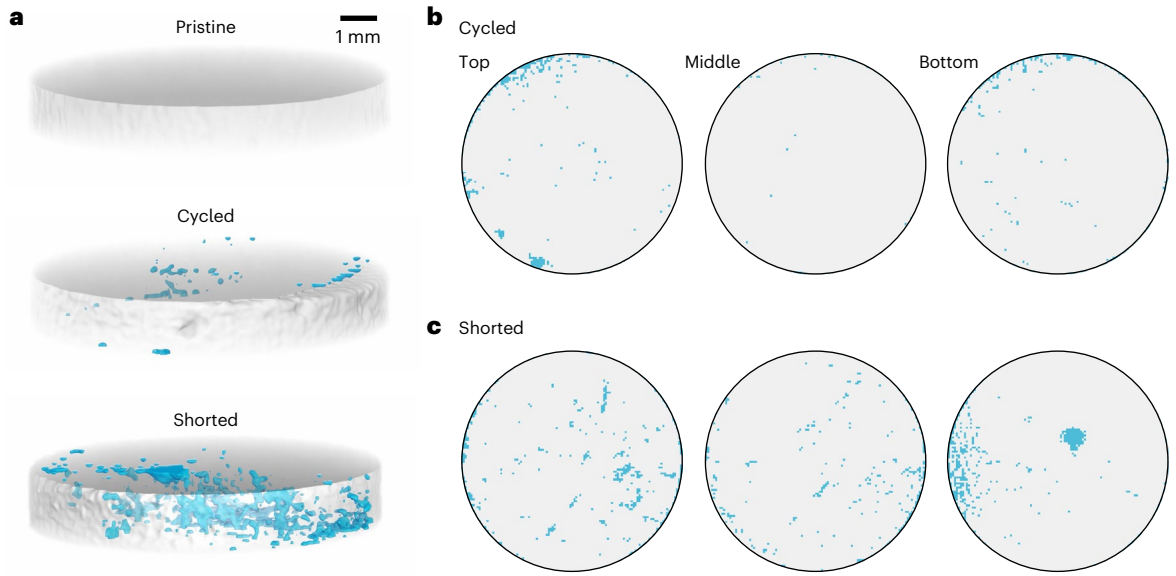

Fig. 3 | Dendrite distribution in LLZO solid electrolytes. a, Volume view of 3D ^{7}Li MRI images of LLZO solid electrolyte pellets and dendrites formed within. From top to bottom are the pristine, cycled without shorting and shorted LLZO. The 3D ^{7}Li MRI images of the LLZO pellets are presented slightly transparently, with the Li microstructure growing within the pellets superimposed and shown in blue. **b**,**c**, Select 2D ^{7}Li MRI cross-sections of cycled (**b**) and shorted (**c**) LLZO (grey) and the dendrites grown within (blue).

In the moderately cycled Li/LLZO/Li battery with a stable voltage profile (Supplementary Fig. 5), we observe clustered Li microstructure formation on the surface of LLZO (Fig. 3a, middle). The two-dimensional (2D) cross-sections (Fig. 3b,c) extracted from the 3D MRI image unveil scattered dendrite spots in the deep bulk of LLZO. The 3D ^{7}Li MRI of the short-circuited Li/LLZO/Li battery (Fig. 3a, bottom) exhibits a dense network of dendrites formed in the LLZO. All the 2D cross-sections (Fig. 3b,c) display signs of dendrites, including small clusters and isolated spots.

In situ monitoring of dendrite formation

We performed in situ ^{7}Li MRI to track the dendrite formation process in real time, using a Li/LLZO/Li battery cell with a natural abundance of Li isotopes. Under a constant current density of 0.1 mA cm^{-2}, the Li/LLZO/Li cell exhibits a steady voltage profile of ~50 mV (Fig. 4a). A slow and gradual increase in voltage is observed due to the loss of interfacial contact and interphase formation[34]. A sudden voltage polarization occurs before a hard short brings the voltage down to 0. Dendrite formation in Li/LLZO/Li is mapped out with in situ fast low-angle shot MRI as a function of cycle time. The dendrites formed at different depths are quantified, and the results are shown in Fig. 4b. Dendrite formation unfolds in distinct stages. In stage I, early dendrite formation emerges in the surface layers 1 and 4, neighbouring the Li metal electrodes. In stage II, minimal dendrite growth occurs in layers 1 and 4, accompanied by the onset of dendrite formation in the middle layers 2 and 3. In stage III, dendrite development in layers 2 and 3 escalates, concurrent with ongoing dendrite growth in the surface layers (1 and 4). In stage IV, towards the point of a short circuit, dendrite formation in layers 2 and 3 begins to decelerate, approaching a plateau. Meanwhile, surface layers 1 and 4 continue to show dendrite growth. The dendrite formation rate at different stages is reflected by the first derivative of dendrite amount with time t, d(dendrite amount)/dt, as shown in Fig. 4c. The surface layers 1 and 4 exhibit rapid dendrite growth at the very beginning of the electrochemical cycling, followed by nearly no dendrite formation in stage II. The middle layers 2 and 3 exhibit prominent rate peaks only in stage III; small ones are visible for stages II and IV. A stalled growth period is observed in stage II. In situ MRI observations confirm a transient pause of dendrite growth following the initial rapid formation, aligning with the results from ex situ NMR (Supplementary Fig. 6).

Initial rapid dendrite formation via plating

To elucidate the insights obtained from NMR, EPR, tracer exchange and MRI, a set of schematics is constructed and displayed in Fig. 4d. At the early stage in the electrochemical cycling of the Li/LLZO/Li cell (stage I), the voltage profile exhibits minimal polarization but with a slight increase in voltage (Fig. 4a) primarily due to increased interfacial impedance[34,35]. The elevation in interfacial impedance mainly originates from the loss of interfacial contact with cycling and interphase formation, as evidenced by our prior studies with MRI[36] and McDowell's work using X-ray imaging[34]. The imperfect interfacial contact between Li metal electrodes and LLZO results in uneven Li stripping and plating. Therefore, small pits form on the Li metal electrode surfaces. Concurrently, protrusions at the contact points grow and penetrate the surface layers of LLZO via grain boundaries (as shown by SEM and TEM; Fig. 1e–i). NMR and EPR results (Fig. 1c,d) support dendrite formation at an early stage, and MRI data (Figs. 3a,b and 4b,c) reveal the rapid formation of protrusions in the surface layers of LLZO. Furthermore, ^{6}Li → ^{7}Li tracer-exchange NMR data reveal that Li^{+} ions are sourced from the LLZO grains at electrode–electrolyte interfaces for the initial dendrite formation via Mechanism 1 (Fig. 2d and Supplementary Fig. 7). The evolution of the NMR and EPR resonances suggests that these initial dendrites are largely amorphous with less electron percolation compared with bulk metallic Li (Fig. 1c,d).

Stalled growth of dendrites

After the initial dendrite formation in the surface layers of LLZO, the dendrites enter a stalled growth period (stage II). In situ MRI displays a quasi-plateau (Fig. 4b) for dendrite formation with a nearly zero growth rate (Fig. 4c), which ex situ NMR confirms (Supplementary Fig. 6). The stalled dendrite formation is likely due to the phase transition from amorphous to crystalline Li dendrite, where a relatively high energy barrier must be overcome before the Li dendrite growth can proceed further into the bulk electrolyte[37,38]. The sharp decrease in the full-width at half-maximum of the ^{6}Li NMR peak from dendrites at the early stages of cycling signifies this amorphous-to-crystalline phase transition

https://doi.org/10.1038/s41563-024-02094-6

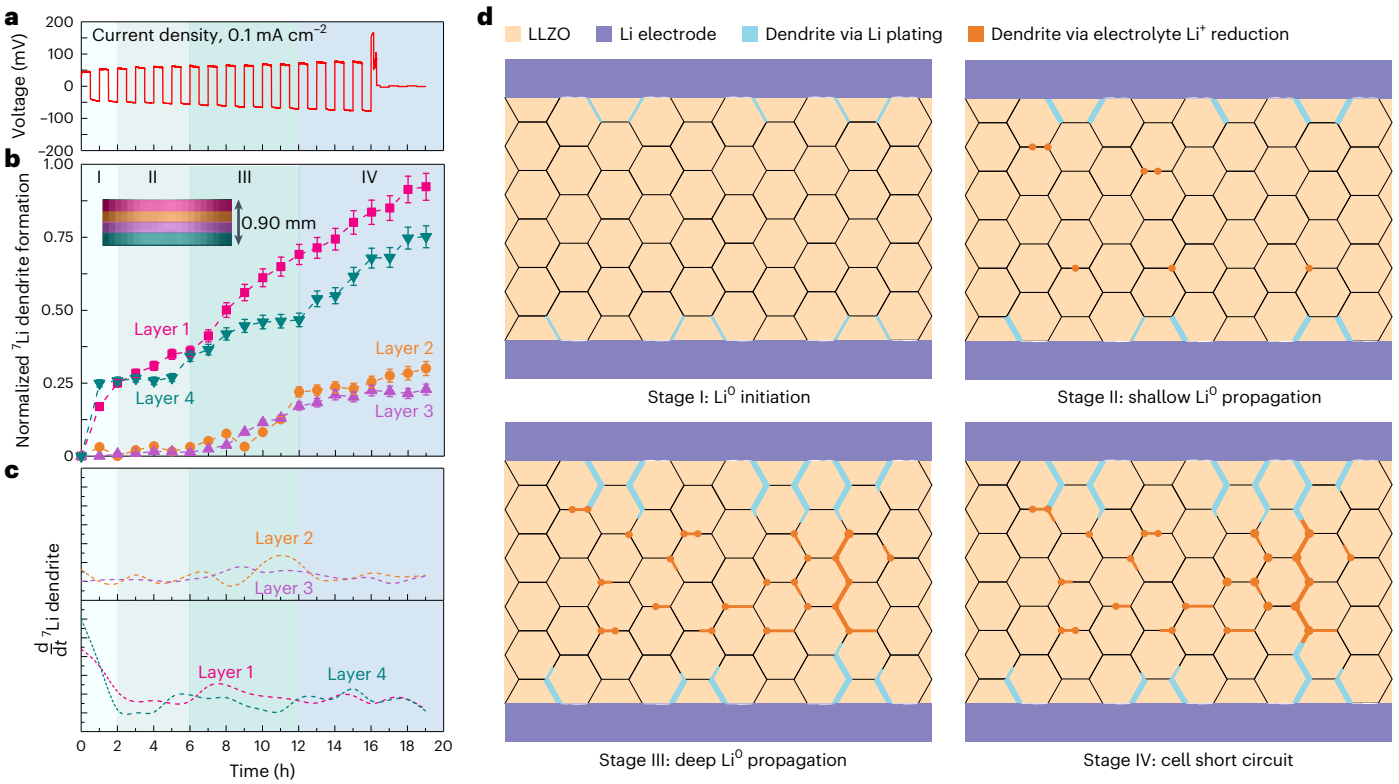

Fig. 4 | In situ MRI detection of dendrite formation and propagation through LLZO. a, Cell voltage profile of a Li/LLZO/Li battery with natural-abundance Li isotopes and cycled with a current density of 0.1 mA cm^{-2}. The shading represents the four stages, labelled in **b**. **b**, Quantified Li dendrite formation at different depths of the LLZO solid electrolyte pellet as a function of cycling time, obtained from quantitative analysis of the in situ ^{7}Li fast low-angle shot MRI data on the Li/LLZO/Li cell. The plots are colour-coded with the corresponding layers of the LLZO pellet, as shown in the inset. The error bars are derived from the signal-to-noise ratio of the images. **c**, Dendrite growth rates (d(Li^{0})/dt) at different depths as a function of cycling time. **d**, Schematic illustrating Li dendrite formation mechanisms and propagation processes in Li/LLZO/Li.

(Supplementary Fig. 8), supported by changes in the Knight shift of the metallic Li NMR resonances (Fig. 1c) and line-widths of the EPR signals (Fig. 1d). This phase transition occurs through the entire battery cycling process amid further formation of amorphous dendrites. The initial crystallization process is most clearly observed in stage II. Such a phase transition is expected to affect the rate of dendrite formation; this partially explains why the dendrite formation is slower in the later stages compared with that in stage I.

Dendrite formation via electrolyte reduction

As dendrite formation slows in the surface layers, it begins in the subsurface and middle layers of LLZO via Mechanism 2 with Li^{+} reduction to form dendrites populating grain boundaries, as observed by TEM (Fig. 1h) and ex situ MRI (Fig. 3). In stage II, isolated dendrite spots start to appear in the middle layers of LLZO, as well as some in the subsurface layers (Figs. 3 and 4b).

Following the stalled growth period in stage II, dendrites flourish rapidly in the middle layers (stage III), as shown by in situ MRI (Fig. 4b,c). The ^{6}Li → ^{7}Li tracer-exchange NMR unveils that dendrite formation in this stage occurs mainly via Li^{+} reduction at grain boundaries (Mechanism 2; Fig. 2d). Based on depth profiling using MRI (Supplementary Fig. 9), no pronounced gradient in the ^{6}Li isotope content across the LLZO pellet retrieved from a battery cell cycled to 30 C is found. Meanwhile, the ^{6}Li → ^{7}Li tracer-exchange process is rather slow at grain boundaries, as suggested by their ^{7}Li-rich content[33] (Supplementary Fig. 3). Furthermore, ex situ NMR shows that the dendrites formed in the middle layers of the electrochemically tracer-exchanged LLZO pellet are predominantly ^{7}Li enriched with non-detectable ^{6}Li content (Fig. 2e), again confirming that dendrite formation in the middle layers of the solid electrolyte is via reduction of Li^{+} at grain boundaries (Mechanism 2).

As dendrites rapidly proliferate within the middle layers of LLZO, top-layer dendrite growth resumes at a relatively swift pace following the amorphous–crystalline phase transition, as revealed by in situ MRI (Fig. 4b,c) and corroborated by ex situ NMR (Supplementary Fig. 6). The overall ^{6}Li isotope abundance in the dendrites continues to decrease (Fig. 2d) due to increased participation of Mechanism 2 for dendrite formation.

Interplay between Li plating and electrolyte reduction

In stage IV, the voltage of Li/LLZO/Li further increases. Eventually, a short circuit occurs after a sudden polarization (Fig. 4a). Dendrite growth slows in the middle layers due to the presence of fewer remaining defects or decreased cell voltage, while remaining rapid in the surface layers (Fig. 4b). Surface layer dendrites formed via Mechanism 1 (Figs. 1e and 3) potentially bridge with those formed in the middle layers via Mechanism 2 (Figs. 2e and 3) to create a percolated network for electron conduction, short-circuiting the battery. Overall, Mechanism 1 dominates the early and late stages of dendrite formation. By contrast, Mechanism 2 is the main mechanism of dendrite formation during the intermediate stages when the cell voltages are relatively high to induce large local potential differences for assisting electron transport and Li^{+} reduction.

The respective contributions of Mechanisms 1 and 2 to overall dendrite formation can vary. The amount of Li dendrites formed via Mechanism 2 depends on several factors, including the local overpotentials, the number and nature of defects in the solid electrolytes and the battery operating conditions. Higher local overpotentials, in

conjunction with a larger number of defects, produce more dendrites formed via Mechanism 2. For instance, with a low current density and thus a low cell voltage of ~5 mV, we observe a negligible fraction of dendrite formation via Mechanism 2, manifested by the larger ^{6}Li isotope abundance of dendrites compared with LLZO. When the cell voltages are increased to 40 mV, the ^{6}Li isotope abundance of dendrites is much smaller than that of LLZO (Supplementary Fig. 10), and an estimate is that >50% of the total dendrites are formed via Mechanism 2.

This work thoroughly investigates dendrite formation in ASSBs using the representative Li/LLZO/Li system. It employs non-invasive NMR, MRI, EPR and tracer-exchange techniques to gain spatial and temporal insights into dendrite initiation and propagation. The quantitative tracer-exchange analysis validates a mechanism of dendrite formation via Li^+ ion reduction at grain boundaries (Mechanism 2), complementing the commonly recognized non-uniform Li plating mechanism (Mechanism 1). The interplay between these mechanisms at various charge states is quantitatively assessed, offering valuable insights for advancing high-performance energy storage technologies.

Online content

Any methods, additional references, Nature Portfolio reporting summaries, source data, extended data, supplementary information, acknowledgements, peer review information; details of author contributions and competing interests; and statements of data and code availability are available at https://doi.org/10.1038/s41563-024-02094-6.

References

1. Harry, K. J., Hallinan, D. T., Parkinson, D. Y., MacDowell, A. A. & Balsara, N. P. Detection of subsurface structures underneath dendrites formed on cycled lithium metal electrodes. *Nat. Mater.* **13**, 69–73 (2014).
2. Cheng, E. J., Sharafi, A. & Sakamoto, J. Intergranular Li metal propagation through polycrystalline $Li_{6.25}Al_{0.25}La_3Zr_2O_{12}$ ceramic electrolyte. *Electrochim. Acta* **223**, 85–91 (2017).
3. Porz, L. et al. Mechanism of lithium metal penetration through inorganic solid electrolytes. *Adv. Energy Mater.* **7**, 1701003 (2017).
4. Krauskopf, T. et al. Lithium-metal growth kinetics on LLZO garnet-type solid electrolytes. *Joule* **3**, 2030–2049 (2019).
5. Manalastas, W. et al. Mechanical failure of garnet electrolytes during Li electrodeposition observed by in-operando microscopy. *J. Power Sources* **412**, 287–293 (2019).
6. Westover, A. S., Dudney, N. J., Sacci, R. L. & Kalnaus, S. Deposition and confinement of Li metal along an artificial Lipon–Lipon interface. *ACS Energy Lett.* **4**, 651–655 (2019).
7. Kazyak, E. et al. Li penetration in ceramic solid electrolytes: *operando* microscopy analysis of morphology, propagation, and reversibility. *Matter* **2**, 1025–1048 (2020).
8. Ning, Z. et al. Visualizing plating-induced cracking in lithium-anode solid-electrolyte cells. *Nat. Mater.* **20**, 1121–1129 (2021).
9. Lv, S. et al. Operando monitoring the lithium spatial distribution of lithium metal anodes. *Nat. Commun.* **9**, 2152 (2018).
10. Ning, Z. et al. Dendrite initiation and propagation in lithium metal solid-state batteries. *Nature* **618**, 287–293 (2023).
11. Krauskopf, T., Hartmann, H., Zeier, W. G. & Janek, J. Toward a fundamental understanding of the lithium metal anode in solid-state batteries—an electrochemo-mechanical study on the garnet-type solid electrolyte $Li_{6.25}Al_{0.25}La_3Zr_2O_{12}$. *ACS Appl. Mater. Interfaces* **11**, 14463–14477 (2019).
12. Tsai, C.-L. et al. $Li_7La_3Zr_2O_{12}$ interface modification for Li dendrite prevention. *ACS Appl. Mater. Interfaces* **8**, 10617–10626 (2016).
13. Heo, S. et al. Short-circuit mechanism induced by crack propagation spurred by inhomogeneous electric field in garnet-based solid electrolyte. *J. Power Sources* **510**, 230389 (2021).
14. Tian, H.-K., Xu, B. & Qi, Y. Computational study of lithium nucleation tendency in $Li_7La_3Zr_2O_{12}$ (LLZO) and rational design of interlayer materials to prevent lithium dendrites. *J. Power Sources* **392**, 79–86 (2018).
15. Tian, H.-K., Liu, Z., Ji, Y., Chen, L.-Q. & Qi, Y. Interfacial electronic properties dictate Li dendrite growth in solid electrolytes. *Chem. Mater.* **31**, 7351–7359 (2019).
16. Zhao, C.-Z. et al. An ion redistributor for dendrite-free lithium metal anodes. *Sci. Adv.* **4**, eaat3446 (2018).
17. Lin, D. et al. Layered reduced graphene oxide with nanoscale interlayer gaps as a stable host for lithium metal anodes. *Nat. Nanotechnol.* **11**, 626–632 (2016).
18. Song, Y. et al. Revealing the short-circuiting mechanism of garnet-based solid-state electrolyte. *Adv. Energy Mater.* **9**, 1900671 (2019).
19. Liu, X. et al. Local electronic structure variation resulting in Li 'filament' formation within solid electrolytes. *Nat. Mater.* **20**, 1485–1490 (2021).
20. Gao, H. et al. Visualizing the failure of solid electrolyte under GPa-level interface stress induced by lithium eruption. *Nat. Commun.* **13**, 5050 (2022).
21. Ye, L. & Li, X. A dynamic stability design strategy for lithium metal solid state batteries. *Nature* **593**, 218–222 (2021).
22. Zhu, C. et al. Understanding the evolution of lithium dendrites at $Li_{6.25}Al_{0.25}La_3Zr_2O_{12}$ grain boundaries via operando microscopy techniques. *Nat. Commun.* **14**, 1300 (2023).
23. Han, F. et al. High electronic conductivity as the origin of lithium dendrite formation within solid electrolytes. *Nat. Energy* **4**, 187–196 (2019).
24. Ping, W. et al. Reversible short-circuit behaviors in garnet-based solid-state batteries. *Adv. Energy Mater.* **10**, 2000702 (2020).
25. Li, Q. et al. *In-situ* visualization of lithium plating in all-solid-state lithium-metal battery. *Nano Energy* **63**, 103895 (2019).
26. Song, B. et al. Dynamic lithium distribution upon dendrite growth and shorting revealed by operando neutron imaging. *ACS Energy Lett.* **4**, 2402–2408 (2019).
27. Murugan, R., Thangadurai, V. & Weppner, W. Fast lithium ion conduction in garnet-type $Li_7La_3Zr_2O_{12}$. *Angew. Chem. Int. Ed.* **46**, 7778–7781 (2007).
28. Richards, W. D., Miara, L. J., Wang, Y., Kim, J. C. & Ceder, G. Interface stability in solid-state batteries. *Chem. Mater.* **28**, 266–273 (2016).
29. Binninger, T., Marcolongo, A., Mottet, M., Weber, V. & Laino, T. Comparison of computational methods for the electrochemical stability window of solid-state electrolyte materials. *J. Mater. Chem. A* **8**, 1347–1359 (2020).
30. Wandt, J. et al. Operando electron paramagnetic resonance spectroscopy – formation of mossy lithium on lithium anodes during charge–discharge cycling. *Energy Environ. Sci.* **8**, 1358–1367 (2015).
31. Niemöller, A., Jakes, P., Eichel, R.-A. & Granwehr, J. EPR imaging of metallic lithium and its application to dendrite localisation in battery separators. *Sci. Rep.* **8**, 14331 (2018).
32. Fang, Q. & Lafdi, K. Effect of nanofiller morphology on the electrical conductivity of polymer nanocomposites. *Nano Express* **2**, 010019 (2021).
33. Hayamizu, K., Terada, Y., Kataoka, K., Akimoto, J. & Haishi, T. Relationship between Li^+ diffusion and ion conduction for single-crystal and powder garnet-type electrolytes studied by ^{7}Li PGSE NMR spectroscopy. *Phys. Chem. Chem. Phys.* **21**, 23589–23597 (2019).
34. Lewis, J. A. et al. Linking void and interphase evolution to electrochemistry in solid-state batteries using operando X-ray tomography. *Nat. Mater.* **20**, 503–510 (2021).

35. Wang, H., Lin, D., Liu, Y., Li, Y. & Cui, Y. Ultrahigh–current density anodes with interconnected Li metal reservoir through overlithiation of mesoporous AlF_3 framework. *Sci. Adv.* **3**, e1701301 (2017).
36. Chien, P.-H. et al. Li distribution heterogeneity in solid electrolyte $Li_{10}GeP_2S_{12}$ upon electrochemical cycling probed by ^7Li MRI. *J. Phys. Chem. Lett.* **9**, 1990–1998 (2018).
37. Yang, M., Liu, Y. & Mo, Y. Lithium crystallization at solid interfaces. *Nat. Commun.* **14**, 2986 (2023).
38. Yang, M., Liu, Y., Nolan, A. M. & Mo, Y. Interfacial atomistic mechanisms of lithium metal stripping and plating in solid-state batteries. *Adv. Mater.* **33**, 2008081 (2021).

Methods

Synthesis of cubic LLZO

Cubic LLZO was prepared using solid-state synthesis. Stoichiometric amounts of LiOH (Sigma-Aldrich, ≥98%, dried at 200 °C for 6 h under dynamic vacuum), La_2O_3 (Sigma-Aldrich, ≥99.9%, dried at 900 °C for 12 h under dynamic vacuum), ZrO_2 (Sigma-Aldrich, ≥99%) and Al_2O_3 (Alfa Asear, ≥99%) with a molar ratio of Li/La/Zr/Al = 7.7:3.0:2.0:0.22 were placed in a 25 ml ZrO_2 jar with two ZrO_2 balls (outer diameter ($Ø_{OD}$) = 10 mm). Acetone (10 ml) was then added as the milling medium. Ball-milling was performed on a SPEX SamplePrep 8000M mixer for three cycles, in which each cycle contained 0.5 h milling followed by 0.5 h resting. Note that excess 10 mol% LiOH was added to compensate for the evaporation of Li during high-temperature sintering. Al_2O_3 was added to stabilize the cubic phase of LLZO. The ball-milled mixture was baked at 50 °C to remove residual acetone. The baked mixture was ground using an agate mortar and pestle before sintering at 800 °C for 20 h in air (ramping at 5 °C min^{-1}). After natural cooling, the mixture was mixed with 5 wt% LiOH per weighted portion (~100 mg) using an agate mortar and pestle for 10 min, followed by a cold press at 3 t or 6 t with stainless moulds (inner diameter ($Ø_{ID}$) = 6 or 10 mm, Across International). The pressed disc was entirely covered by its mother powders without touching the Al_2O_3 crucible during sintering at 1,100 °C for 6 h to ensure the formation of LLZO. After cooling, the sintered LLZO pellet was sequentially polished using sandpaper (150-grit, 800-grit and 1,500-grit papers) until shiny surfaces were observed by the naked eye. The obtained LLZO pellet, after polishing, has dimensions, depending on the moulds, of 8.9 ± 0.1 mm (4.8 ± 0.1 mm) in diameter and 1.2 ± 0.1 mm (1.0 ± 0.1 mm) in thickness. The relative density of LLZO pellets investigated in this study was ~90%.

Assembly of symmetric cells

All the following tasks were performed in an Ar-filled glove box. Li chips (MTI Corporation) were scratched gently with a spatula, pressed at 1 t and punched with a hollow die ($Ø_{ID}$ = 8 or 4 mm). This process is employed to reduce the thickness of Li metal electrodes (vide infra). The polished LLZO pellets were sandwiched with two freshly prepared Li chips and pressed in stainless moulds to improve the contact of LLZO–Li interfaces. Polyethylene films were inserted as a barrier to prevent direct contact between Li chips and stainless die during pressing. The Li/LLZO/Li cell was then subjected to heat treatment at 175 °C for 30 min under a dynamic vacuum followed by natural cooling. These symmetric cells were subject to ex situ 3D ^{7}Li MRI experiments. For ex situ tracer-exchange NMR experiments, similar Li/LLZO/Li symmetric cells were used in which the Li metal electrodes were prepared using ^{6}Li chunks (Sigma-Aldrich, 95 at.% ^{6}Li). For operando 2D ^{7}Li MRI experiments, bag cells were assembled by attaching two Cu strips (60 mm long by 3 mm wide) onto the surface of the Li metal of the freshly prepared Li/LLZO/Li cell. The Cu/Li/LLZO/Li/Cu bag cells were hermetically sealed in a heat-sealable polyester bag.

Electrochemistry

The d.c. polarization of Li/LLZO/Li cells was carried out with home-built cylindrical cells[36] on an Arbin battery testing system. Small LLZO pellets ($Ø_{OD}$ = 6.8 ± 0.1 mm) were polarized at 0.1 mA cm^{-2} to observe the formation of Li microstructures. The current direction was reversed every 30 min, and a 5 min idling was inserted between charge and discharge. Post-mortem analysis on the cycled small LLZO pellets was carried out with SEM, ^{7}Li NMR and EPR. Before measurements, Li metal was completely removed from the Li/LLZO/Li cells by polishing the surfaces with sandpaper (800-grit and 1,500-grit papers) in an Ar-filled glove box. Cycled LLZO pellets were then crushed into powders or pieces using an agate mortar and pestle. Large LLZO pellets ($Ø_{OD}$ = 8.9 ± 0.1 mm), which were the specimens for the ex situ 3D ^{7}Li MRI studies, were purposely polarized at 0.1 mA cm^{-2} and 0.5 mA cm^{-2} to induce the formation of Li microstructures without and with shorting, respectively. The current direction was reversed every 30 min, and a 5 min idling was inserted between charge and discharge. Polarization of the Cu/Li/LLZO/Li/Cu bag cells for in situ 2D ^{7}Li fast low-angle shot MRI experiments was carried out on a Gamry Reference 600$^+$ with a step mode, in which a charge–discharge cycle was polarized at 0.1 mA cm^{-2}.

MRI

The 3D ^{7}Li MRI was conducted on an 11.75 T magnet (Larmor frequency ($\omega_0/2\pi$) = 194.4 MHz for ^{7}Li; Magnex Scientific) with an 89-mm-wide bore at the College of Engineering on the joint Florida A&M University and Florida State University campus. To ensure the integrity of the LLZO–Li interfaces as well as the embedded Li microstructure in LLZO, we kept both the LLZO that was cycled without shorting and the shorted LLZO pellets sandwiched by Li metal electrodes and aligned the orientation of the LLZO pellets in parallel with both the $\mathbf{B}_0$ and $\mathbf{B}_1$ magnetic fields, described below. Micro2.5 gradients (Bruker Corp) were employed in these experiments. A flip angle of 90°, an echo time of 1 ms and a repetition time of 0.25 s were used. The 3D images were collected with a field of view of 10 mm × 10 mm × 3.2 mm (matrix = 100 × 100 × 32). For each 3D image 128 averages were accumulated, with a total acquisition time of 26.4 h. The 3D ^{7}Li MRI volume images were processed with MATLAB scripts to generate 2D cross-sections, side views and projections. These images were also subject to histogram analysis performed on ImageJ (National Institutes of Health).

In situ 2D ^{7}Li fast low-angle shot[39] MRI experiments were performed on a home-built 21.1 T ultra-wide-bore magnet ($\omega_0/2\pi$ = 394.7 MHz for ^{7}Li) at the National High Magnetic Field Laboratory. Supplementary Scheme 1 shows the experimental set-up for in situ MRI acquisitions. A custom-built MRI coil (Supplementary Scheme 1a) is the central modification, which allows secure placement of the solid-state battery (Supplementary Scheme 1a) inside the imaging coil with the preferred orientation to both the external magnetic field $\mathbf{B}_0$ generated by the magnet and the magnetic field $\mathbf{B}_1$ generated by the NMR coil for spin polarization. Such a configuration of battery placement is critical to achieving high-fidelity MRI imaging by eliminating eddy current effects[40]. A gradient of 60 G cm^{-1} in three orthogonal directions (Resonance Research) was employed in these experiments. A flip angle of 30° with an echo time of 0.918 ms and a repetition time of 0.3 s were used. The 2D images were collected with a field of view of 17 mm × 11 mm (matrix = 81 × 52). For each 2D image 1,024 averages were accumulated before and after cycling, with a total acquisition time of 4.5 h. All 2D ^{7}Li MRI images and histogram analyses were processed on ImageJ (National Institutes of Health).

Solid-state NMR

The ^{7}Li MAS NMR spectra on LLZO (pristine and cycled) were acquired on a Bruker DRX-830 spectrometer (19.6 T, $\omega_0/2\pi$ = 322.57 MHz for ^{7}Li) with a home-built 1.8 mm probe spinning at 25 kHz. All ^{7}Li spectra were acquired using a spin-echo pulse sequence with a π/2 pulse length of 2 μs (radio frequency = 125 kHz) and a recycle delay of 1 s. The ^{7}Li chemical shift was calibrated with dry LiCl(s) at −1.1 ppm.

For tracer-exchange NMR experiments, ^{6}Li and ^{7}Li MAS NMR spectra on LLZO were acquired on a Bruker DRX-830 spectrometer (19.6 T, $\omega_0/2\pi$ = 122.14 MHz for ^{6}Li, and 322.57 MHz for ^{7}Li) with a home-built 3.2 mm probe spinning at 14 kHz for ^{6}Li and 13 kHz for ^{7}Li. The latter was spinning a bit slower to avoid the overlap of the sidebands from the LLZO peak and metallic Li peak at around 264.5 ppm. All spectra were acquired using a single-pulse sequence with a recycle delay of 10 s for ^{6}Li and 2 s for ^{7}Li. The measurements were conducted on three battery cells for each data point. The ^{6}Li or ^{7}Li chemical shift was calibrated with LiCl(s) at −1.1 ppm. For quantification, a calibration factor of 28.45, determined from the ^{6}Li and ^{7}Li NMR of naturally abundant LiCl(s), was used to correct for the ^{6}Li and ^{7}Li NMR sensitivity difference in the isotope composition calculations of dendrites and solid electrolytes.

EPR

EPR measurements were conducted at 240 GHz with a continuous wave heterodyne EPR spectrometer constructed at the National High

Magnetic Field Laboratory with submillimetre waves propagating through cylindrical wave guides instead of a resonant cavity and signals detected by a liquid-helium-cooled InSb bolometer (QMC Instruments). The magnetic field was modulated with a lock-in amplifier by phase-sensitive detection. Hysteresis and field nonlinearity corrections were applied. The spectra were collected from 8.53 to 8.585 T with a sweep rate of 0.201 mT s^{-1} at 290 K and an average of four scans.

Powder X-ray diffraction

To verify the phase purity of LLZO, powder X-ray diffraction was carried out at room temperature on a Philips X'Pert powder X-ray diffractometer operating at 45 kV and 40 mA. The powder X-ray diffraction pattern (wavelength, $\lambda = 1.5406$ Å, Cu Kα) was acquired under step mode with a scanning time of 0.5 s per 0.02° step from 10 to 70° (2θ, the angle between the transmitted beam and reflected beam).

SEM

The morphology on the cross-sections of a cycled LLZO pellet was investigated using a field-emission SEM instrument (NOVA NanoSEM 400) operating at 15 kV and a working distance of 5.9 mm with an Everhart–Thornley detector. To reduce the exposure of LLZO to moist air, the broken pieces of LLZO pellets were mounted on the SEM holder in an Ar-filled glove box before transferring to the SEM chamber.

TEM

High-resolution TEM and energy-filtered TEM images were collected on a JEOL JEM2100F microscope with a working voltage of 200 kV. The TEM samples were prepared in the glove box. The LLZO pellets were ground into powder and directly dropped on a Cu grid, then quickly transferred to the holder and microscope (exposure of the samples to air was controlled to be less than 30 s).

Data availability

Data generated or analysed during this study are also included in Supplementary Information. Further data are available from the corresponding authors upon request. Source data are provided with this paper.

Code availability

The Python code used for simulating the tracer-exchange process is provided via GitHub at https://github.com/Jak1022/Python_tracer_exchange.

References

39. Haase, A. Snapshot FLASH MRI. Applications to T1, T2, and chemical-shift imaging. *Magn. Reson. Med.* **13**, 77–89 (1990).
40. Serša, I. & Mikac, U. A study of MR signal reception from a model for a battery cell. *J. Magn. Reson.* **294**, 7–15 (2018).

Acknowledgements

We acknowledge the support from the National Science Foundation under grant no. DMR-2319151 for Y.C. and Y.-Y.H. All solid-state NMR experiments were performed at the National High Magnetic Field Laboratory, which is supported by National Science Foundation Cooperative Agreement nos DMR-1644779 and DMR-2128556. We thank the US Department of Energy (DOE), Office of Science, Office of Basic Energy Sciences programme for support under award no. DE-SC0019121 for D.H. and H.X. This research used resources of the Center for Nanoscale Materials, a DOE Office of Science User Facility operated for the DOE Office of Science by Argonne National Laboratory under contract DE-AC02-06CH11357.

Author contributions

Y.-Y.H. conceived the concept, designed the experiments and supervised the project. S.C.G. directed and supervised the MRI component of the study. H.L., Y.C. and P.-H.C. performed LLZO synthesis, X-ray diffraction characterization, symmetrical cell assembly and electrochemical measurements. H.L., Y.C., P.-H.C. and E.T. carried out ^{6,7}Li NMR. H.L. and Y.C. performed numerical simulations and Li isotope composition analysis of cycled samples. S.C.G., J.T.R., H.L., Y.C., P.-H.C., G.A., I.P.O., J.B., S.W.H. and Y.-Y.H. performed MRI and data analysis. P.L.G. developed the MRI gradient coil for in situ 2D MRI. D.H. and H.X. contributed to TEM and energy-filtered TEM data acquisition and analysis. Y.-Y.H., H.L., Y.C. and P.-H.C. wrote the paper with contributions from all co-authors.

Competing interests

The authors declare no competing interests.

Additional information

Supplementary information The online version contains supplementary material available at https://doi.org/10.1038/s41563-024-02094-6.

Correspondence and requests for materials should be addressed to Samuel C. Grant or Yan-Yan Hu.

Peer review information *Nature Materials* thanks the anonymous reviewers for their contribution to the peer review of this work.